FlatChem 51 (2025) 100872

Contents lists available at ScienceDirect

FlatChem

journal homepage: www.sciencedirect.com/journal/flatchem

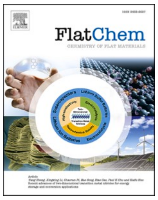

Effective photocatalytic behaviour of tungsten disulphide (WS_2) with multi and fewer layers for degradation of methylene blue

Lizzie Mampane [a,b], Bulelwa Ntsendwana [b,d,*], William Moloto [b], Sivuyisiwe Mapukata [b], Themba Ntuli [b], Nosipho Moloto [a], Lucky Sikhwivhilu [b,c,*]

[a] School of Chemistry, University of the Witwatersrand, Private Bag 3, Wits, 2050, South Africa
[b] DSTI/Mintek Nanotechnology Innovation Centre, Advanced Materials Division, Mintek, Randburg, 2125, South Africa
[c] Department of chemistry, Faculty of science and engineering and Agriculture, University of Venda, Private Bag X5050, Thohoyandou 0950, South Africa
[d] Centre for NanoEngineering and Advanced Materials, School of Mining, Metallurgy and Chemical Engineering, University of Johannesburg, Johannesburg 2006, South Africa

ARTICLE INFO

Keywords:
Photocatalysis
WS_2
Methylene blue
Reusability
Band gap

ABSTRACT

The tungsten disulphide nanosheets (WS_2) nanosheets have an exceptional ability to degrade hazardous organic pollutants due to strong UV and visible light absorption. Hence, WS_2 nanosheets, which exhibited varying layers, were synthesized to study the influence of the number of layers and colour on the photocatalytic degradation of organic pollutants. The synthesized WS_2 multi and few-layer layers were systematically characterized to determine structural, morphological, and optical properties. The as-synthesized materials were tested as photocatalysts toward the degradation of methylene blue (MB) as a target pollutant in simulated water. The multilayered WS_2 and few-layered WS_2 exhibited strong photocatalytic activity, with 99 % MB degradation efficiency in less than 30 min at pH 10.3. However, the few-layered WS_2 demonstrated high stability after the fourth run, with an efficiency of more than 90 % and a decrease of 4 %. It was concluded that few-layered WS_2 nanosheets are ideal photocatalyst materials due to the enhanced light absorption, recyclability, and photocatalytic activity in comparison with multi-layered WS_2 nanosheets.

1. Introduction

The significant development in globalization and industrialization is the two main causes of environmental pollution. Rapid urbanization, shifting consumer behaviours, population growth, and quicker socioeconomic development have all contributed to an increase in water pollution in the environment [1,2]. Water pollution is one of the world's most prevalent pollutants, and there is an urgent need to eliminate contaminants from water bodies using new scientific technology advancements [2]. Additionally, the concentration of pollutants, particularly organic pollutants, dyes, and other dangerous substances, has increased in the water bodies, however, this has a negative impact on both aquatic life and human health [3]. Industrial effluent water from the agrochemical, paper, and pharmaceutical industries are a common source of non-biodegradable and hazardous pollutants [4]. Methylene blue (MB), a cationic thiazine dye commonly used in the chemical and biological industries, can induce a variety of health concerns, including vomiting, nausea, excessive perspiration, restless breathing, eye discomfort, and mental abnormalities.

Photocatalysis is an effective method of removing a wide spectrum of contaminants [5]. It generates radicals from solar energy (*hv*) to oxidize these contaminants and catalyze their breakdown. Currently, many studies have been undertaken on the photocatalytic activity of different nanostructures. Metal oxide semiconductors, such as TiO_2 and ZnO, are the most investigated photocatalysts; however, their wide bandgap restricts their UV, as they only capture 5 % of total sunlight [6]. The number of defects on nanostructured materials can be minimised to improve their energy conversion efficiency [7]. In nanostructured photocatalysts, the semiconductor is discrete; when energy exceeds the threshold for semiconductor absorption of light, the valence band (VB) and the conduction band (CB) separate from one another, causing the carrier separation of the semiconductor material and the interband transition of valence electrons to produce photoelectrons and holes [8].

After the discovery of graphene, various two-dimensional (2D) semiconductor materials were employed for photocatalytic reactions [9]. These materials offer superior physical qualities [10]. Transition

---

* Corresponding author at: DSTI/Mintek Nanotechnology Innovation Centre, Advanced Materials Division, Mintek, Randburg, 2125, South Africa.
E-mail addresses: bulelwan@mintek.co.za (B. Ntsendwana), LuckyS@mintek.co.za (L. Sikhwivhilu).

https://doi.org/10.1016/j.flatc.2025.100872
Received 20 February 2025; Received in revised form 14 April 2025; Accepted 28 April 2025
Available online 29 April 2025
2452-2627/© 2025 Elsevier B.V. All rights are reserved, including those for text and data mining, AI training, and similar technologies.

metal dichalcogenides (TMDs) have inspired interest in optoelectronics and catalysis since the 1970s. Due to their intriguing optical properties and surface chemistry. TMDs are composed of S-M-S layers with strong intramolecular interactions but low interlayer contacts due to van der Waals forces [11]. Their unique electrical, mechanical, and optical qualities have made them suitable for a wide range of applications. Among other TMDs, WS_2 nanosheets, as emerging 2D materials, have recently attracted a lot of attention as catalysts due to their remarkable optical properties and monolayer or few-layer surface chemistry. However, few layers possess additional properties as compared to their bulk counterparts, this is due to the confinement effect [12]. The WS_2 nanosheets are corrosion-resistant with a noticeable bandgap and offer unique features such as high surface area, excellent photocatalysts, good electrochemical activity, promising electrical characteristics, high mobility, and biocompatibility.

In recent years, various WS_2-based photocatalysts have been used in the removal of pollutants in wastewater [13,14]. Fatima and co-workers used WS_2 to degrade and detect pharmaceutical waste, and 90 % of the antibiotic nitrofurantoin (NFT) was degraded [15]. Xie and co-workers photodegraded rhodamine B (RhB) with highly dispersed WS_2 nanosheets, and high efficiency was observed [16]. The research focuses on improving the WS_2 performance through metal doping and the formation of heterojunction photocatalysts. Properties such as bandgap and electronic structure and improving absorption and charge carrier separation at the surface. Huang and co-workers employed WS_2 and MoS_2 monolayers as co-catalysts in the hybrids to improve photocatalysis performance and the results enhanced optical absorption in the region of the ultraviolet-visible light [17]. Alhmanzani and co-workers used a heterostructure of InS/WS to degrade various parabens in water, and results show good photodegradation efficiency of more than 88.6 % of the pollutants were degraded in 90 min [18]. Shende and co-workers used a ternary composite WS_2/GO/Au photodegraded 99 % MB for 90 min [19]. Overall, these studies demonstrate the significant potential of WS_2-based photocatalysts for various organic contaminants in water. The high photodegradation efficiency, ranging from 88 to 90 %, was observed, with the heterostructures or hybrid systems exhibiting excellent photodegradation performance. These findings highlight the viability of WS_2 as a key component in the development of advanced photocatalysts for environmental remediation applications.

Different synthesis methods have been employed to improve the bandgap and the number of layers. Several techniques have been employed for the synthesis of WS_2 nanosheets, such as the chemical synthesis method [20], Pulse laser deposition [21] and ball milling CVD [22]. However, their requirement of high temperature and complex systems restricts control number of control layers and size [23]. A combination of these techniques improves the material properties. Koinkar and co-workers used laser ablation in the liquid environment to reduce WS_2 micro sheets into free-standing nanosheets [24], Koinkkar and co-workers used a hydrothermal method and incorporated TiO_2 and Au to improve photocatalytic properties [25], On the other hand, femtosecond pulse laser was used to produce fewer layers of WS_2 [26].

The novel and superior characteristics of ultrathin two-dimensional (2D) materials with graphene analogue, sustained research interest for a considerable time. In particular, the exfoliated and free-standing nanosheets of WS_2 are noteworthy. Various exfoliation techniques, including mechanical cleavage and chemical exfoliation, have been employed; however, these methods may modify the material properties and result in the creation of lattice defects [27,28]. The presence of lattice defects may introduce unwanted electronic states, reduce charge carrier mobility and hinder effective charge separation, ultimately resulting in poor photodegradation efficiency. Hence, a lot of research has been focusing on alternative methods that can produce fewer lattice defects, thereby enhancing the photocatalytic properties. Ratha and a co-worker synthesized a few layers of WS_2 through a chemical (liquid) synthesis method at 265 °C for 24 h, which is a long time for synthesis [29]. Furthermore, the thermal solid-state synthesis technique has been reported as a method that can produce exfoliated nanosheets, which have the potential for scaling up and producing high-quality free-standing layers with fewer defects. Gajić and co-workers used the solid-solid phase reaction to synthesize WS_2 nanosheets by heating WO_3 powder and thiourea in a nitrogen environment at 850 °C. Similarly, Zhang and co-workers also synthesized ultrathin WS_2 via a facile solid phase reaction method using WO_3 and thiourea at 850 °C for 1 h [30] These methods minimise the lattice defects and enhance the photocatalyst activities.

There have been efforts to combine both liquid and solid-based methods to further improve the material properties. Koinkar and co-workers used laser ablation in the liquid environment to reduce WS_2 micro sheets into free-standing nanosheets [24], Koinkkar and co-workers used a hydrothermal method and incorporated TiO_2 and Au to improve photocatalytic properties [25], On the other hand, a femtosecond pulse laser was used to produce fewer layers of WS_2 [26]. Despite the advancements, there is still a challenge in developing a simple, reproducible, and cost-efficient synthetic approach to generate ultrathin WS_2 nanosheets. In this study, we have optimised reaction conditions (resident time, low temperature), which resulted in the formation of WS_2 multilayer and few-layer nanosheets using the solid-state thermal synthesis method. The nanosheets displayed different colours and numbers of layers, demonstrating promising photocatalytic degradation of methylene blue. In this research study, A detailed comparative analysis was conducted to evaluate the photocatalytic characteristics of multilayered (G-WS_2) in comparison to few-layered (B-WS_2).

2. Materials and methods

2.1. Materials

Methylene blue was purchased from Sigma SA. Tungsten oxide (WO_3) and Thiourea (CH_4N_2S, 98 %) were obtained from ACE Merck, hydrochloric acid (HCl) and sodium hydroxide (NaOH) were obtained from MERCK. All required chemicals were of analytical grade.

2.2. Synthesis of WS_2 nanosheets

Thermal solid-state synthesis of WS_2 nanosheets was adopted from Zhang and co-workers [31] and it was modified. In this study and WS_2 was achieved at a very low temperature of 600 °C, which is lower than what is reported in the literature. The first step, 1 mmol tungsten trioxide and 60 mmol thiourea were mixed in a mortar, and then the mixture was placed into a crucible. The temperature of a tube furnace was raised to 600 °C at a rate of 10 °C/min. The residence time was varied from 2 to 4 h. The products obtained at 2 h were grey in colour and the one at 4 h was black in colour. The obtained product was washed thrice with ethanol and then washed with DI water to remove any impurities. The final sample was dried at 60 °C for 8 h. Sample naming was as follows: prefix colour and suffix is tungsten sulphite: i.e. G-WS_2 and B-WS_2.

2.3. Characterization of the as-synthesized nanosheets

The morphology of the catalysts was studied by high-resolution transmission electron microscopy (TEM). Phase identification was observed by X-ray diffraction (XRD) using Cu Kα X-ray radiation ($\lambda = 1.5418$ Å). UV–Vis spectroscopy (UV–Vis) was performed to observe the photocatalytic activity of the WS_2 nanosheets against MB at a wavelength of 665 nm with a scan range of 550 to 750 nm. Functional groups and bonds were detected by FTIR. The surface area and pore size distribution of WS_2 nanostructures were determined experimentally by Brunauer–Emmett–Teller (BET) analyses. Nitrogen adsorption-desorption isotherms were measured at 77.4 K.

2.4. . Procedure for photocatalysis

The as-synthesized catalyst was utilized to degrade MB under a 300 W xenon lamp that was placed around 30 cm away. To investigate the photocatalytic degradation mechanism of MB, 20 mg photocatalytic samples were added to 40 mL of a 200 mg/L MB solution, WS_2 samples in comparison to the G-WS_2 and B-WS_2 as catalysts. The solution was initially magnetically agitated for 30 min in the dark to obtain the adsorption–desorption balance. UV–Vis absorption spectra were recorded every ten minutes for G-WS_2 and B-WS_2 and every 30 min, with the first sample collected at 0 min and deionized water used as a contrast. The concentration of MB was determined using Lambert-Beer's law. The photocatalytic efficiency eq. (1):

$$\eta(100\%) = \frac{C}{C_0} \times 100\% = \frac{A}{A_0} \times 100\%. \quad (1)$$

where C_0 is the concentration before the reaction, and C is the concentration obtained 10 min after the reaction. A_0 is the absorbance before the reaction, while A is the absorbance measured at (0, 5,10,15,30 and 60 min) during the reaction.

A study compared the light degradation of G-WS_2 and B-WS_2 nanostructures against MB. A 200 mg/L solution containing 20 mg of each catalyst was produced and agitated for half an hour in the dark. Then, WS_2 photo catalyst was added and mixed. In the ambient atmosphere, a dark blue solution was generated with a visible light wavelength of 665 nm from a 300 W Xe lamp. For 60 min, 5 mL of solution was obtained at (0, 5,10,15,30 and 60 min) time intervals, with the initial sample taken at 0 min representing the sample after 30 min in the dark. The pH (1.3, 7.15 and 10.3) and loading of the catalyst (20, 40 and 60 mg) as factors affecting photo degradation were investigated.

3. Results and discussion

3.1. Characterization

3.1.1. TEM for WS_2 Nano sheets

Scanning and transmission electron microscopy SEM and TEM were used to characterize the microstructures and morphologies of G-WS_2 and B-WS_2. The SEM images are displayed in Fig. 1(a and b). It is evident that the G-WS_2 in Fig. 1(a) is made up of dense layered structures and B-WS_2 shows less dense sheet-like materials, as shown in Fig. 1(b). The TEM images are presented in Fig. 1(c and d). TEM confirms the sheet-like morphology observed in the SEM images. The TEM images also confirm that the B-WS_2 nanosheets are very thin and appear transparent under electron beam irradiation, further validating the sheet-like morphology observed in SEM. It is worth noticing that the resulting G-WS_2 nanosheets are extremely thick, as shown in Fig. 1(c) and B-WS_2 nanosheets appear to be thin and appear transparent under electron beam irradiation, as shown in Fig. 1(d).

As residence time increased, the lateral and vertical dimensions increased; however, ultrathin nanosheets of B-WS_2 are stacked randomly and appear transparent under the electron beam's irradiation, implying that the obtained B-WS_2 nanosheets are very thin. This is in agreement with what was reported in the literature [32].

3.1.2. XRD and FTIR for WS_2 nanosheets

The FTIR spectra of WS_2 samples synthesized at different residence

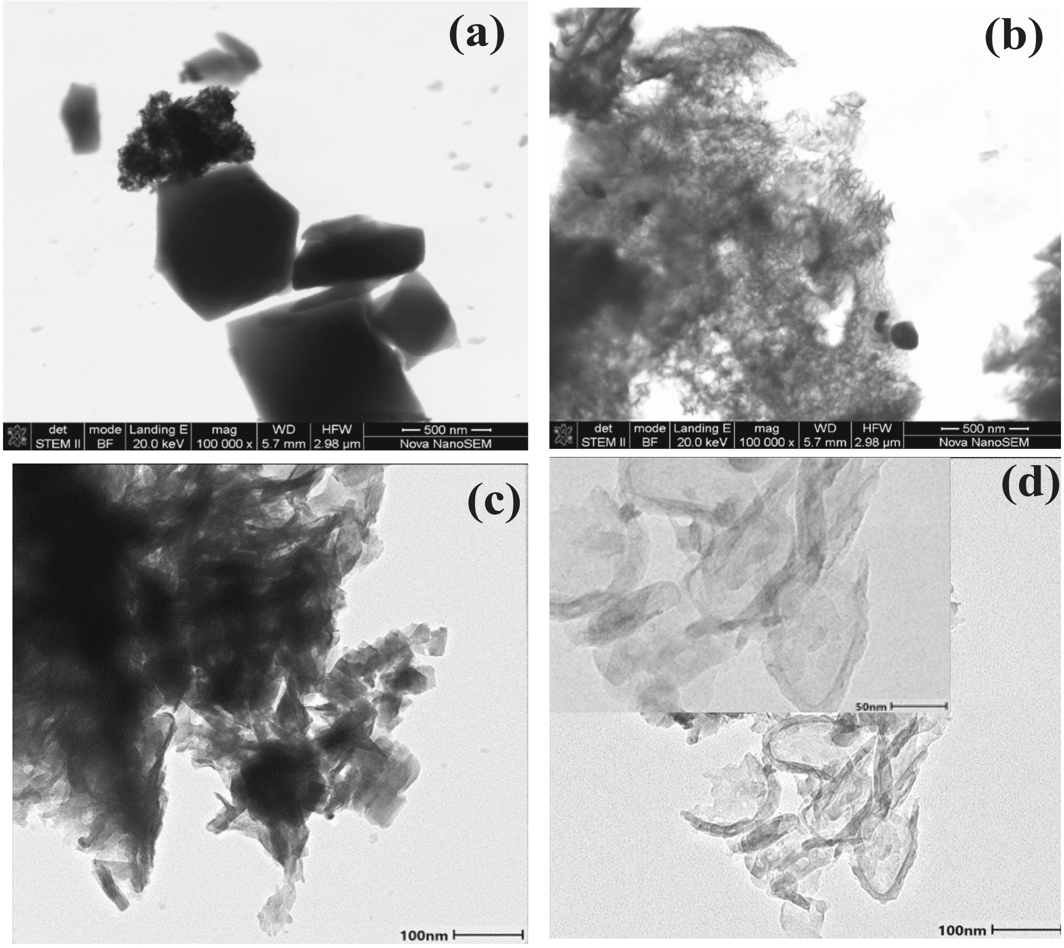

Fig. 1. (a) and (b) SEM images of G-WS_2 and B-WS_2, respectively; and TEM images of G-WS_2 and B-WS_2 ((c) and (d)), respectively.

times are illustrated in Fig. 2(a). Several peaks associated with significant vibration bands of tungsten disulfide were observed in both samples G-WS_2 and B-WS_2, i.e., vibration bands around 3208 $cm^{-1,}$ which match the stretching and bending vibration spectrum of W—S. It is obvious that the W—S bond is present [33]. Apart from the normal peak of bound ambient moisture content stretching vibration bands of -OH at 3208 and 2884,2998,1640, 1407 cm^{-1} [34]. The characteristic absorption bands at 1070, 805 and correspond to the S—S and W—S stretching vibrations [35]. For sample B-$WS_{2,}$ a new vibration peak appeared at 616 cm^{-1}, which corresponds to S—$S_,$ due to the additional load of sulphur as the residence time was prolonged. This confirms the formation of WS_2 nanosheets.

The XRD spectra in Fig. 2(b) for samples synthesized at 2 h and 4 h the spectra have similar crystallinity more amorphous. At a residence time of 2 h, it shows that the WS_2 structure is formed. The characteristics peaks at round 15.20°, 26.57°, 27.88°, 28.88,38.38°, 40.10°, 43.72°, 47.59,56.54,63.30,64.70 and 69.90°, were indexed to (002), (0 0 4), (100), (101), (1 0 0),(102), (0 0 6), (1 0 5), (1 0 6)(110),(112) and (200), respectively. WS_2 crystal structure with a group space P63/mmc. The index was adopted from JCPDS No.: 08–0237. However, as residence time increases from G-WS_2 and B-$WS_{2,}$ the peaks broaden and a shift to higher theta angles, which might be due to the sheet rearrangements as more removal of the CO_2, NH_2 and OH during the sulfurization reaction of WO_3 [36] as well as the thermal exfoliation of the sheets that occurred due to an increase in residence time [37]. The main tungsten disulphide peaks, which are consistent throughout from G-WS_2 and B-WS_2, were indexed at (200), (002), (004), and (105) [38]. This is in agreement with previous reports in the literature [39,40]. The average S–W–S interlayer distance (d) value was evaluated using the diffraction peak (002) at 2ϴ = 27.56^0 and 27.88^0 for G-WS_2 and B-$WS_{2,}$ respectively, using Debye-Scherer Eq. (2).

$$d = \frac{0.9\lambda}{\beta\cos(\theta)} \tag{2}$$

where d is the interlayer distance, λ is the radiation wavelength (1.5406 Å), θ is the diffraction angle, and β is the full width at half maximum.

The d spacing for G-WS_2 was estimated to be 126.5 nm, which is approximately twice as much as the d spacing of 64.9 nm of B-WS_2. The value of the d spacing of B-WS_2 is close to the one reported in literature for Exfoliated WS_2 nanosheets are mono-layered or few-layered [41]. and the d spacing of G-WS_2 corresponds to a multi-layer structure [42].

3.1.3. Raman shifts analysis of the as-synthesized WS_2 at different residence times

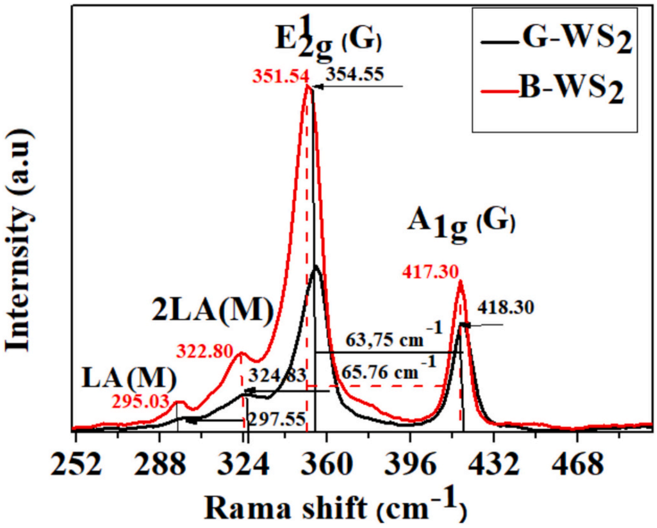

Fig. 3. Raman spectra of the as-synthesized WS_2 at different residence times.

Table 1
The intensity ratio (E^1_{2g} /A1g) G-WS_2 and B-WS_2.

Material	E^1_{2}g	A1g	E^1_{2}g/A1g
G-WS_2	14,883.23	10,517.99	1.415
B-WS_2	29,021.94	13,753.29	2.110

In Raman shift used to characterize the structural properties of the WS_2 nanomaterial synthesized at different residence times is illustrated in Fig. 3 and Table 1. First order resonance of the bulk $WS_{2,}$ two characteristic peaks of the Raman active mode, the A1g occurs around 419 cm^{-1}, which is due to the out-of-plane vibration of sulphur atoms and the E^1_{2g} mode occurs around 352 cm^{-1}, corresponding to the in-plane displacement of both sulphur and tungsten atoms [43]. The exfoliations of the sheets can be monitored by the redshift in the A1g mode, which is due to the lattice relaxation phenomenon as the number of layers decreases [44]. Additionally, the number of sheets can be estimated by the ratio of E^1_{2g} /A1g [45,46]. The decrease in the ratio corresponds to the increase in the number of layers. When the E^1_{2g} /A1g is greater than 2.2, it corresponds to monolayers, E^1_{2g} /A1g less than 0.47 correlates to the form of bulk WS_2, and when E^1_{2g} /A1g is between 0.47 and 2.2, this signifies the presence of few-layer WS_2 [46]. Table 1 shows the summary of the Raman peaks intensity ratios of G-WS_2 and B-WS_2.

The E^1_{2g} /A1g ratios of G-WS_2 and B-WS_2 were calculated to be 1.415 and 2.11, respectively. This confirms that B-WS_2 has a smaller number of layers as compared to G-WS_2. However, both samples seem to have layers of WS_2. Thus, 2.1 (B-WS_2) has than 3 layers [47] and 1.4 (G-WS_2) consists of less than 5 layers [48]. This confirms that G-WS_2 is a multi-layered structure and B-WS_2 is a fewer-layer structure.

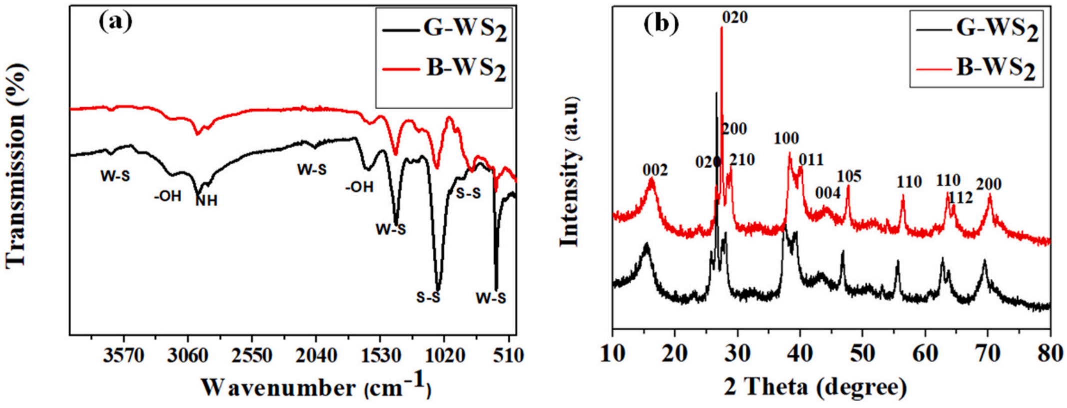

Fig. 2. (a) FTIR and (b) XRD spectra of the a-synthesized WS_2 at different residence times.

3.1.4. BET analysis for WS_2 Nano sheets

The specific surface area of the as-synthesized-G-WS_2 and B-WS_2 nanosheets was obtained by the Brunauer–Emmett–Teller (BET) technique via nitrogen adsorption–desorption isotherms as shown in Fig. 4 (a), the measured specific surface areas BET, samples G-WS_2 and B-WS_2 are 8.241, and 9.197 m^2/g, respectively. The WS_2 nanosheets synthesized at different residence times exhibit a mesoporous nature. The IV type form of isotherms with an H_3-type hysteresis loop ($P/P0 > 0.4$) [49], following the International Union of Pure and Applied Chemistry (IUPAC) Nomenclature. Furthermore, a considerable decrease in WS_2 samples' adsorption capacity with increasing residence time was observed.

The prepared G-WS_2 and B-WS_2 pore size distribution is presented in Fig. 4 (b), and Table 2 shows the summary BET analysis of all the samples. The pore size ranges from 5 to 50 nm, with averages of 26.2 and 17,6 nm, respectively. This suggests the coexistence of mesoporous structures in the WS_2.

3.1.5. UV–vis DRS and PL analysis of G-WS_2 and B-WS_2

The band gap energies of all WS_2 samples synthesized at different residence times were determined using the Tauc plot. This is very important to examine the photo-physical and photo-chemical properties of the material this properties of material are well documented in literature since 1966 when Tauc proposed the way to utilise optical absorption spectra to estimate the band gap energies to reveal their photocatalytic properties and Davis and motto, developed the method further, due to the assumptions in Tauc's methods, the photon energy is directly proportional to the coefficient (α) The absorption can be expressed by the following Eqs. (3).

$$(\alpha.hvv)^{0.5} = B\left(hv - E_g\right) \tag{3}$$

$$\left(F(R_\infty) = \frac{K}{S} = \frac{(1 - R_\infty)}{2R_\infty} \right. \tag{4}$$

$$(F(R_\infty).hv\,)^{0.5} = B(hv - Eg) \tag{5}$$

Where, h is the Planck constant, ν is the photon's frequency, Eg is the band gap energy, and B is a constant. The band gap energy is usually determined from diffuse reflectance spectra. According to the theory of P. Kubelka and F. Munk presented in 1931. The measured reflectance spectra can be transformed to the corresponding absorption spectra by applying the Kubelka–Munk function (F(R∞), Eq. (3), and finally, substitute the coefficient (α) of absorption with the (F(R∞), and Eq. (4) was used to estimate the energy band gap using reflectance [50].

Fig. 5(a) illustrates the band gap energies of samples synthesized at 2 and 4 h. The band gap energies increase with the increase in residence time. The G-WS_2 and B-WS_2 exhibited band gaps of 1.8 and 2 eV, respectively. As the thermal exfoliation takes place, the band gap increases. A similar trend was reported in the literature [51,52]. The band gap energy of (1.8 eV) G-WS_2 synthesized at low residence time is comparable to the multi-layer WS_2 bandgap [53]. However, as residence time increased to 4 h, the WS_2 band gap increased (2.0 eV), which correlated to fewer layers, and this confirms that the exfoliation took place [51]; [54].

PL analysis was utilized to determine the optical properties of the as-synthesized WS_2 nanosheets. Fig. 5(b) shows the PL of G-WS_2 and B-WS_2 excitation wavelength of 317 nm for both samples. Photoluminescence plots reveal three separate characteristic emission peaks. It is noteworthy that the PL spectra' main peak at around 432.04 nm was fixed for all the samples, with the shoulder peaks at around 400 and 460 nm, which may be attributed to a quantum-confined transition in the WS_2 nanosheets [53]. The fixed peak at 432.04 nm shows that the PL characteristics do not change with the increase in the thermal sulfurization period. The emission intensity increased with prolonged residence time. This was attributed to the decrease in the number of atomic layers and suggests exfoliation toward free-standing or thin layers [55]. To evaluate the PL behaviour of the as-synthesized the Full-width-at-half maximum (FWHM) and the shift of the peak at around 460 nm were used. The PL peak of the B-WS_2 sample is broader with FWHM 88.27 nm and is redshifted by 1.9 nm compared to the PL peak of the G-WS_2 sample, which exhibited a FWHM of 84.43 nm. This suggests a greater degree of exfoliation toward thinner. The PL analysis is in agreement with the calculated energy band gaps from UV. This was previously reported in the literature for the exfoliation of bulk WS_2 using chemical methods [56]; [55].

Fig. 5(c) illustrates the UV–Vis spectra of G-WS_2 and B-WS_2 with the absorption in the range of 200–900 nm. Typically, the emergence of characteristic excitonic absorption bands in the visible range is expected for WS_2 multilayered and exfoliated nanosheets, excitonic absorption caused to the small size effect [57]. The fewer layers of WS_2 absorb in the slightly higher wavelength than multilayers. Both G-WS_2 and B-WS_2 have their excitonic peaks appear as the most prominent absorption features in the near-UV region ($\lambda \approx 300$ nm) for the as-prepared nanosheets. This significant absorption is attributed to transitions occurring from the low-lying valence band to the conduction band in the exfoliated WS_2 nanosheets, which is near 320 nm and can be explained by the quantum size effect. Similar behaviour of WS_2 nanosheets was reported

Table 2
BET analysis of G-WS_2 and B-WS_2.

Material	Specific surface area m^2/g	Pore diameter (Å)	Pore volume(Å)
G-WS_2	8.241	268.56	0.052
B-WS_2	9.197	174.53	0.040

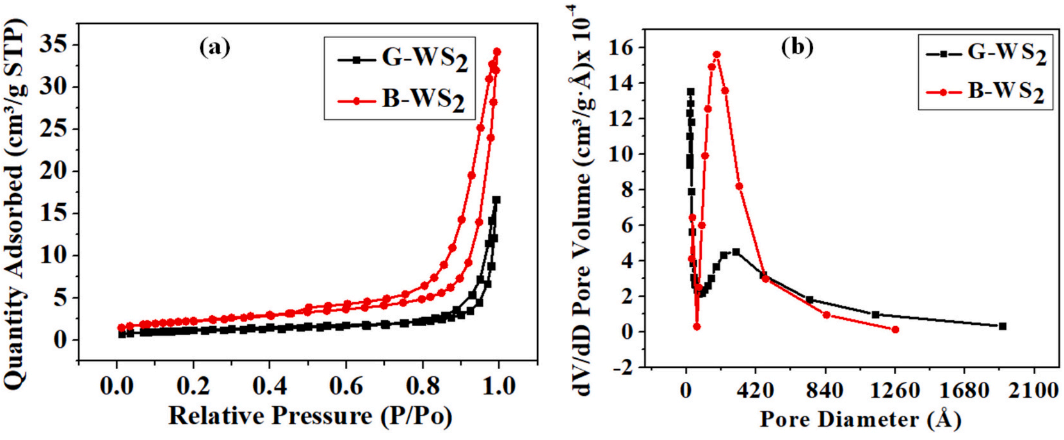

Fig. 4. The BET and pore volume analysis of the as-synthesized WS_2 at different residence times.

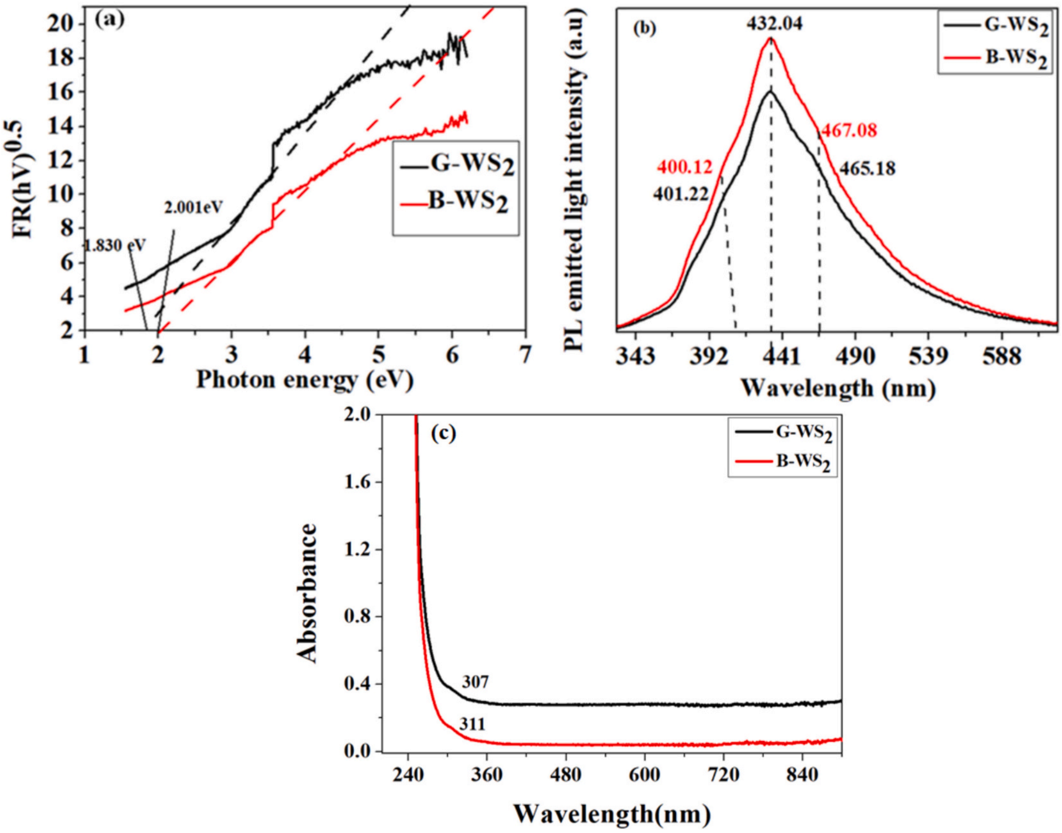

Fig. 5. The band gap energy estimated through the Tauc's plot and (b) PL relationship of as-synthesized WS_2 nanosheets at an excitation wavelength of 317 nm (c) the UV–Vis absorbance spectra of the as-synthesized WS_2 nanosheets.

by Sharma and co-workers [58].

3.2. Photocatalytic degradation of MB under UV light

3.2.1. Effect of initial concentration on photocatalysts

The dark adsorption-desorption phenomenon was investigated for MB adsorption on the surfaces of G-WS_2 and B-WS_2 photocatalysts for 30 min, by detecting the usual MB peak in UV–vis analysis 665 nm wavelength. Fig. 6 shows the photo degradation capabilities of G-WS_2 and B-WS_2. The image demonstrates the photocatalytic breakdown of initial MB concentrations (300,250, and 200 mg/L), with 20 mg of G-WS_2 and B-WS_2 of the photocatalyst. Samples were collected at $t = 0$, 5, 10, 15, 30, and 60 min to investigate time-dependent photocatalytic MB degradation. Where t = 0 corresponds to the sample of adsorption-desorption in the dark after 30 min.

The dark adsorption-desorption equilibrium spectra for both photocatalytic materials reveal that MB adsorption on the catalyst surface decreases as the starting concentration increases, reaching equilibrium after 30 min, as illustrated in Fig. 6(a, c and d), the surface adsorption efficiency in the dark was determined to be 72.50 %, 80.35 %, and 85.45 for G-WS_2, on concentration 300,250 and 200 mg/L, respectively. The degradation of 200,250 and 300 mg/L on B-WS_2 in Fig. 6(b, d and e), was found to be 76.99 %, 81.00 %, and 92.75 %, based on adsorption-desorption equilibria of B-WS_2, which outperformed G-WS_2. Table 3 shows the degradation efficiency calculated using Eq. (5).

$$\eta = \left(1 - \frac{C}{C_0}\right) \times 100 \tag{6}$$

Where η is efficiency, C is the intensity at a time 't' and C_0 is the intensity at time 't0'.

Results show that low concentration exhibits fast degradation at 200 mg/L, with a catalysis loading of 20 mg, at times $t = 5$,10, 15,20,30 and 60 min are 85.45 %, 95.00 %, 95.06 %,97.50, 97.50 and 97.50 % for G-WS_2, respectively. Similarly, the efficiencies obtained for B-WS_2, are 92.71 %, 99.50 %, 99.75 %, 99.78 %, 99.96 and 99.98 % respectively.

3.2.2. Kinetic and the mechanism

Fig. 7(a and b) depicts a plot of relative absorbance (C/C_0) vs. time for different MB concentrations, with G-WS_2 in Fig. 7(a) and B-WS_2 in Fig. 7(b). The B-WS_2 is more efficient in photodegrading dye solutions than G-WS_2. C/C_0 denotes the intensity at time's' vs the intensity at time 't_0'. As shown in Fig. 2(a and b), ~ 95.0 and 99.8 % of the dye was degraded in the first 15 min for G-WS_2 and B-WS_2, respectively. It was found that B-WS_2 had a greater rate constant than G-WS_2. Additionally, this shows that the response rate slows down as increasing concentration increases, which may be due to the less penetration and amplified light scattering [59].The photocatalytic degradation at very low concentration is characterized by pseudo-first-order rate kinetics, as described in eqs. (6 and 7).

$$C = C_0 e^{-kt} \tag{7}$$

$$-\ln(C/C_0) = kt \tag{8}$$

Where "k" is the rate constant of the reaction and "C" is the concentration. Absorption intensity at time "t," where "C0" is the initial absorbance at 0 min, and "t" is the time. The rate constant of the reaction can be obtained by graphing time against −ln(C/C0), and the corresponding slope can also be determined.

A graph of $-\ln(C/C_0)$ against time can be used to determine the apparent rate constant, k (decolourization process's rate). As the concentration increases from 200 to 300 mg/L, the apparent rate constants for both WS_2, G, and WS_2, B decreased. These rate constants are presented in Table 4 for all initial MB concentrations. The concentration is inversely proportional to the reaction rate [60]. Additionally, this shows

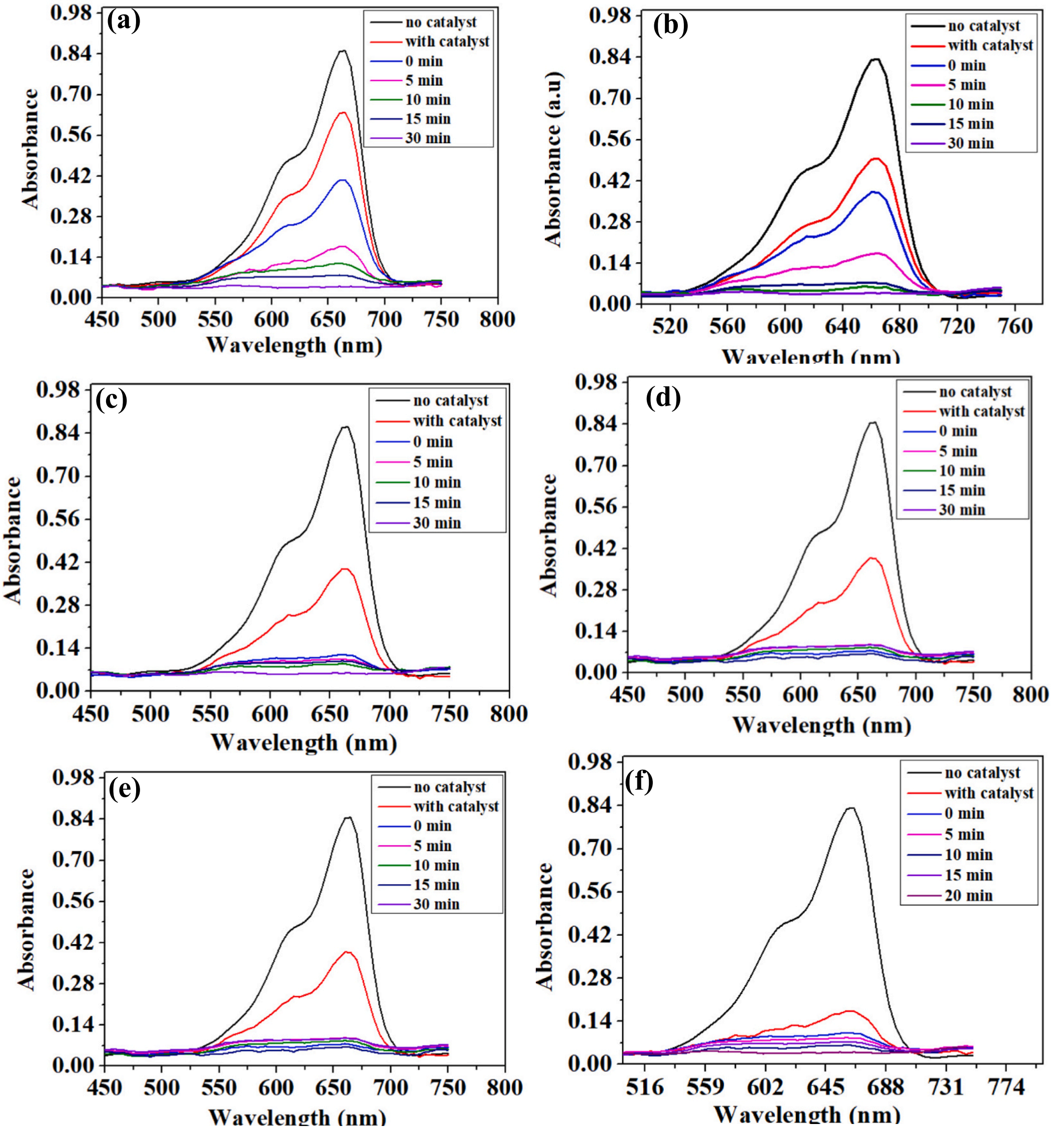

Fig. 6. The surface photo degradation of initial concentrations of MB (200,250 and 300 mg/L) with 20 mg of catalyst at pH of 7.15. (a, c and e) for G-WS_2 and (b, d, and f) for B-WS_2.

Table 3
The degradation efficiency of G-WS_2 and B-WS_2 with time for a concentration of 200 mg/L at 20 mg catalyst loading.

Time (min)	%degradation (G-WS_2)	%degradation (B-WS_2)
−30	85.45	92.71
5	87.50	99.50
10	95.00	99.75
15	95.06	99.78
20	97.50	99.96
30	97.50	99.98
60	97.50	99.98

that the response rate slows down at increasing concentration [61]. Photocatalytic degradation efficiency at very low concentration followed the first-order kinetics model. The rate constants for B-WS_2 and G-WS_2 at an initial concentration of 200 mg/L were found to be 0.0906 min^{-1} and 0.0701 min^{-1}, respectively, based on the kinetic curve shown in Fig. 7(c and d). The rate constant of B-WS_2 was observed to be higher than that of G-WS_2; this might be due to the colour (black) and the high band gap enhances photo-catalytic performance as compared to grey [62] as one of the factors. The Raman $E_{12}g/A_1g$ ratio was found to be 2.1 for B-WS_2, compared to 1.4 for G-WS_2, while bandgap analysis revealed values of 2.0 eV for B-WS_2 and 1.8 eV for G-WS_2. The exfoliated WS_2 nanosheets (B-WS_2) have a high surface area, which offers abundant active sites, and exhibit increased interactions between the photo-generated electron-hole pair and MB dye molecules. Furthermore, the increase in bandgap in the few layers is due to their quantum confinement effect, which, along with surface area, enhances the photocatalytic efficiency. The quantum confinement increases the energy band gap as the number of layers decreases in WS_2 nanosheets. For bulk or multi-layer WS_2, the band gap is indirect, where the electrons and holes are not easily able to recombine [20]. However, in monolayer or few-layer WS_2, the material undergoes a transition from an indirect to a direct bandgap, which is crucial for many photocatalytic applications. The reduced thickness of the material confines the charge carriers, leading to enhanced optical and electronic properties [21].

At a high methylene blue (MB) concentration of 300 mg/L, intense competition among MB molecules for active sites on the catalyst surface occurs, potentially hindering the photocatalytic degradation efficiency, the rate constants were low, measuring 0.026 min^{-1} for G-WS_2 and 0.040 min^{-1} for B-WS_2, with R^2 values for pseudo-first-order kinetics

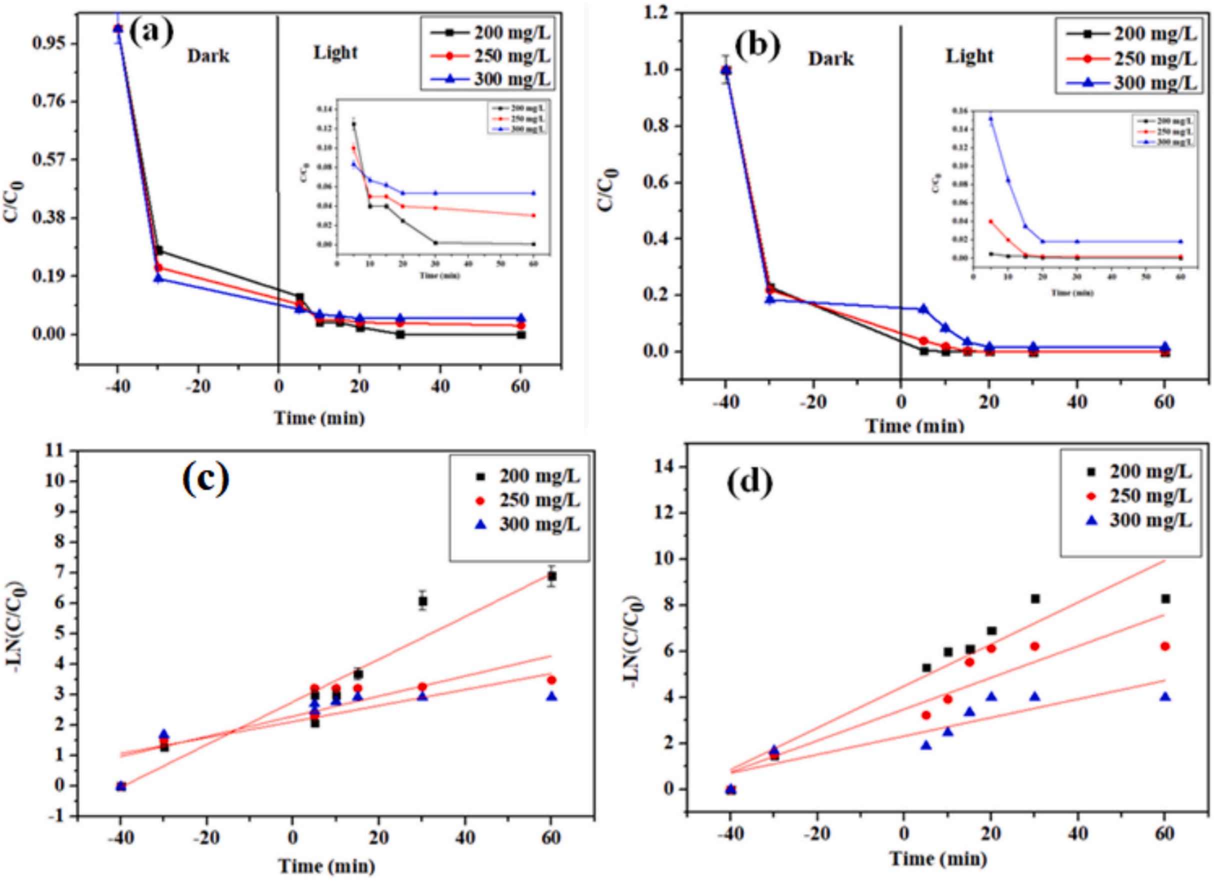

Fig. 7. (a and b) relative absorbance (C/C_0) vs. time plot and (c and d) $-\ln(C/C_0)$ vs time of G-WS_2 and B-WS_2, respectively.

Table 4
Photocatalytic Performance: first-order kinetics.

Concentration	Rate constant G-WS_2 ($K = min^{-1}$)	R^2	Rate constant B-WS_2 ($K = min^{-1}$)	R^2
200 mg/L	0.07006	0.90	0.0906	0.90
250 mg/L	0.03304	0.70	0.0683	0.82
300 mg/L	0.02626	0.40	0.04013	0.61

being 0.40 for G-WS_2 and 0.61 for B-WS_2 at the same concentration. This could be attributed to the saturation of photocatalytic active sites on the surface, resulting in a reduced degradation rate, which may also impair light penetration. Furthermore, B-WS_2 demonstrated higher efficiency than G-WS_2, achieving equilibrium in degradation after 30 min.

3.2.3. *Effect of pH on photocatalysts*

A negatively charged material surface enhances the degradation of methylene blue (MB) dye, especially in basic pH conditions. This is because the positively charged MB dye is attracted to the negatively charged surface, leading to increased adsorption and ultimately faster degradation. Optimal degradation is often observed at pH values above the point of zero charge (PZC) of the material, where the surface is more negatively charged. The effect of pH on MB degradation was studied in the pH range of 1.3 to 10.3, using a 200 mg/L MB dye concentration, and 20 mg catalyst loading was evaluated in Fig. 8. Table 5 shows a summary of the surface charge of the catalyst and the point of zero charge. Furthermore, both G-WS_2 and B-WS_2 display a negatively charged surface potential at pH 7, with zeta potential measurements ranging from −15.4 to −15.9 mV, respectively. These findings indicate a favourable charge interaction with MB dye, as MB is characterized as a cationic dye. This is due to the positively charged MB dye being easily attracted to the

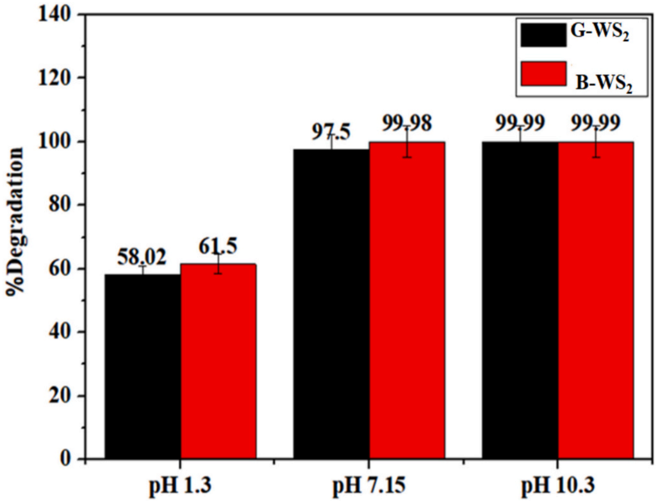

Fig. 8. Photodegradation efficiency of MB at different solution pH (concentration- 200 mg/L, catalyst mass 20 mg, and volume 40 mL) of G-WS_2 and B-WS_2.

Table 5
The summary zeta potential, surface charge and point of zero charge data.

Material	Conductivity (mV)	Zeta potential (mV)	Zeta deviations (mV)	PZC
G-WS_2	0.0216	−15.46	4.89	1.9
B-WS_2	0.0247	−15.93	5.75	2.67

surface of a negatively charged catalyst through electrostatic interactions [63]. This enhanced compatibility increases the adsorption capacity of MB on the catalytic surface, which could lead to better photocatalytic performance [64]. Optimum degradation was observed at pH above the point of zero charge of both G-WS_2 and B-WS_2. The point of zero charge (pH_{ZPC}) for G-WS_2 and B-WS_2 was 2.47 and 1.90, respectively. When the pH falls below the pH_{ZPC} of the catalyst, the surface of the catalyst becomes positively charged, hence, low degradation efficiency [65]. However, when the pH exceeds pH_{ZPC}, the catalyst becomes negatively charged [66]. MB is a cationic dye; therefore, it is attracted to the catalytic surface of G-WS_2 and B-WS_2 between pH 7.15 and 10.3 [67]. As a result, photocatalytic degradation was found to be higher in more alkaline environments as compared to acidic environments.

According to the Coulombic forces, the repulsion of both negatively charged photocatalyst surfaces and hydroxide anions, may prevent the production of ·OH ions, which assists in the degradation of the cationic dyes [67,68]. The degradation efficiency increased by 42 % from pH 1.3 to 10.3 for G-WS_2. At high pH, the degradation of MB by B-WS_2 reached completion. However, at low pH only 62 % of the dye was degraded. Further photocatalytic investigation was carried out at the optimal pH of 10.3.

3.2.4. *Effect of loading of the catalyst on photocatalysts*

The discoloration increases with an increase in catalyst loading. There are no isosbestic spots in the optical absorbance of the solution for either catalyst, indicating that the MB has been completely degraded without the formation of intermediate complexes [69]. *As shown in* Fig. 9(a, c and d) degradation efficiency vs time plot shows the efficiency of 97.50 %,96.90 %, and 94.99 % using 20 mg, 40 mg, and 60 mg of the G-WS_2 photocatalyst, respectively.

Comparably, Fig. 9(b, d, and f) shows the same catalyst loading for B-WS_2, with corresponding efficiency values of 99.98 %, 98.99 %, and 98.00 %, respectively. The high photodegradation efficiency of MB was achieved with B-WS_2 nanosheets (Table 6). However, as the loading increased from 40 mg to 60 mg, no change in the degradation efficiency was observed. Therefore, the optimum loading for all the catalysts was 40 mg.

Table 6
Photo degradation efficiency on the loading of G-WS_2 and B-WS_2.

Time (min)	%degradation (G-WS_2)			%degradation (B-WS_2)		
	20 mg	40 mg	60 mg	20 mg	40 mg	60 mg
−30	85.45	73.00	71.95	92.71	76.98	77.20
5	87.50	82.50	85.95	99.50	87.87	88.88
10	95.00	87.50	89.15	99.75	89.12	89.80
15	95.06	92.87	90.98	99.88	97.51	98.75
20	97.50	95.98	93.99	99.96	98.55	99.77
30	97.50	97.99	97.99	99.98	99.97	99.98
60	97.50	98.99	98.00	99.98	99.98	99.99

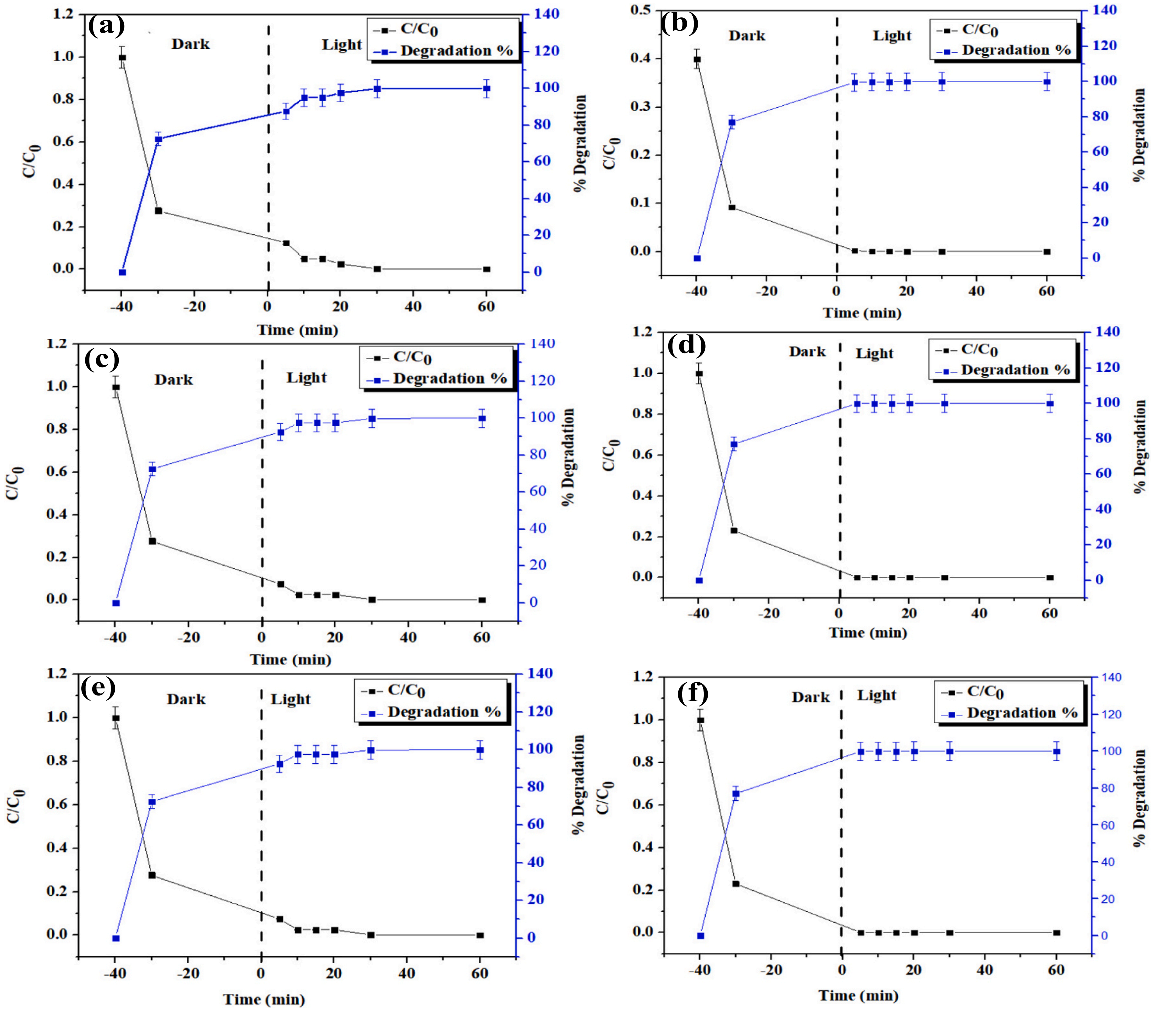

Fig. 9. Dosage loading of the photocatalyst (a and b), 20 mg, (c and d), 40 mg, and (e and f) 60 mg for G-WS_2 and B-WS_2, respectively.

3.3. *Comparative study of the degradation efficiency*

A comparative study was conducted to evaluate the performance of various WS_2 photocatalysts for methylene blue (MB) degradation, as reported in the literature, against the WS_2 synthesized in this study. The summary of this comparison is presented in Table 7. In this work, WS_2 nanosheets were thermally exfoliated using a solid-state synthesis method at different residence times to investigate their dye photodegradation performance. The degradation efficiencies of G-WS_2 (98.3 %) and B-WS_2 (99.8 %) observed in this study are significantly higher than those reported in previous studies. Literature reports indicate degradation efficiencies of 15 %, 93 %, 50 %, and 85 %, with corresponding band gaps ranging from 1.4 to 2.6 eV for multi-layer WS_2 synthesized using hydrothermal methods with an autoclave and chemical vapor deposition (CVD). However, the WS_2 used in this study for MB photodegradation under visible light demonstrated superior efficiency, outperforming the reported values in the literature. This observation suggests that the unique properties of WS_2 synthesized via the solid-state method, especially the exfoliated or few-layer B-WS_2, significantly contributed to its enhanced photocatalytic performance.

3.3.1. *The mechanism of degradation*

Fig. 10 presents the photodegradation mechanism for both G-WS_2 and B-WS_2 nanosheets. The photodegradation mechanism occurs in three main steps, i.e., 1) the generation of an electron-hole pair, 2) redox reaction and 3) finally, the degradation of pollutants using the OH radicals. Eqs. 4 to 8 describe the photocatalysis mechanism in detail. The generation of electron–hole pairs in the photodegradation mechanism involves the migration of an electron (e−) from the valence band to the conduction band, leaving behind a hole (h^+), as described by Eq. (5). This mechanism occurs when the photocatalyst (WS_2 nanosheets) is exposed to photons with energy equal to or greater than the photocatalyst's bandgap energy (Eg). Additionally, Eq. (6) shows that these holes (h^+) combine with water molecules to produce an h^+ ion and a hydroxyl radical (OH•) [74]. On the other hand, when oxygen molecules react with the electrons, the superoxide ions (O_2^-) are created [75] in Eq. 7. In addition, these superoxide anions produce the superoxide anion radical ($O_2^{\cdot}$) through electron loss. According to eqs. (8) and (9) h^+ ions and the superoxide anion radical ($O_2^{\cdot}$) react to produce H_2O_2, which then transforms into the hydroxyl radical (OH•) [76]. Fig. 10 shows the degradation mechanism.

$$WS_2 + hv \rightarrow e^- + h^+ \tag{9}$$

$$H_2O + h^+ \rightarrow OH^{\cdot} + H^+ \tag{10}$$

$$O_2 + e^- \rightarrow O_2^- \tag{11}$$

$$O_2^- - + 2H^+ \rightarrow H_2O_2 \tag{12}$$

$$H_2O_2 + e^- \rightarrow OH^{\cdot} + OH^- \tag{13}$$

3.3.2. *Photostability and reusability*

Fig. 11(a) shows the FT-IR before and after MB degradation; a noticeable peak shift to the lower wave number was observed in both G-WS_2 and B-WS_2 nanosheets after the photodegradation of MB dye. The peaks at 1464 and 2947.20 cm^{-1} correspond to the C═C and N—H stretching vibrations in MB after adsorption onto the surface of WS_2. For G-WS_2, new peaks appeared, which were attributed to the transformation of MB molecules into intermediate products. Additionally, peaks at 2101, 1168 and 754 cm^{-1} were identified, attributed to the C═O asymmetric stretching of CO_2, C═O stretching of aldehyde, and S—O stretching of sulphate ions (SO_4^{2+}). The observed new peak at 754 cm^{-1} corresponds to the vibration stretching of S—O and CO, indicating that the G-WS_2 formed various intermediates, which were competing with MB for active sites, leading to a decline in photodegradation efficiency. However, in the case of B-WS_2, only the CO_2 peak was observed, indicating the formation of CO-based byproducts, which are less toxic, confirming mineralization. This shows that B-WS_2 degraded the MB completely without forming intermediate products. it can be concluded that the high surface area of B-WS_2 contributes to providing active sites for the reaction between electron-hole pairs and MB molecules. This enhances the degradation process and improves the photocatalytic performance.

To test reusability, G-WS_2 and B-WS_2 were washed with de-ionized water and oven-dried for 12 h at 50 °C. The same method was carried out for each run. Fig. 11(b) depicts the photo stability and reusability of G-WS_2 and B-WS_2 for MB photodegradation across four consecutive runs under ideal reaction conditions (200 mg/L of MB, pH of 10.3 and 40 mg of photocatalyst). The photodegradation efficiencies of B-WS_2 were 99, 97, 95, and 95 % for the first, second, third, and fourth runs, respectively; the efficiency decline is minor between runs. In a contract with G-WS_2, efficiency dropped by 10 % after the third run, from 97 to 84 %. The slightly higher reduction in photocatalytic effectiveness may be attributed to the adsorption of MB onto the pores and layers.

4. Conclusion

The synthesis of multi-layer and fewer layers of WS_2 nanosheets, denoted G-WS_2 and B-WS_2, was successfully synthesized using solid-state thermal synthesis techniques. Both G-WS_2 and B-WS_2 exhibit strong photocatalytic activity, with 99 % MB degradation in less than 30 min at pH 10.3 and 40 mg of photocatalyst. The photodegradation efficiency of G-WS_2 and B-WS_2 kinetics indicated that the reactions followed pseudo-first-order kinetics. However, the rate of degradation of B-WS_2 was faster than that of G-WS_2; this could be attributed to the fact that B-WS_2 has a high specific surface area, bandgap due to the small size effect, hence photodegradation was faster. Furthermore, photodegradation studies demonstrated excellent photocatalytic activity in very alkaline medium, pH $\geq$ 7.15, which is due to the coulombic repulsion between the negatively charged photocatalyst surface and the hydroxide anions. The reusability tests show that B-WS_2 is highly stable even after the fourth run, with an efficiency of more than 90 % and a decrease of 4 %. In a contract with G-WS_2, after the fourth run, efficiency decreased by 10 %. This approach is cost-effective, reproducible, and feasible for upscaling and is used in industrial effluent water remediation.

Table 7

Comparative study of the photocatalytic performance on the degradation of MB on WS_2 Photocatalyst.

Catalyst	Optimum catalyst loading	Pollutant	Reactor (light source)	Time (min)	Bad gap (eV)	Degradation Efficiency (%)	Ref.
WS_2	5 mg	MB	5 W LED bulb,	120	1.41	15	[70]
WS_2-PANI	20 mg	MB	Visible light	90	2.6	93	[71]
WS_2	20 mg	MB	100 mW/cm2 from xenon arc lamp	60	1.3	50	[72]
WS_2	50 mg	MB		150	1.9	85	[73]
G-WS_2	40 mg	MB	300 xenon lamp.	60	1.8	98.99	This study
B-WS_2	40 mg	MB	300 xenon lamp.	60	2.1	99.99	This study

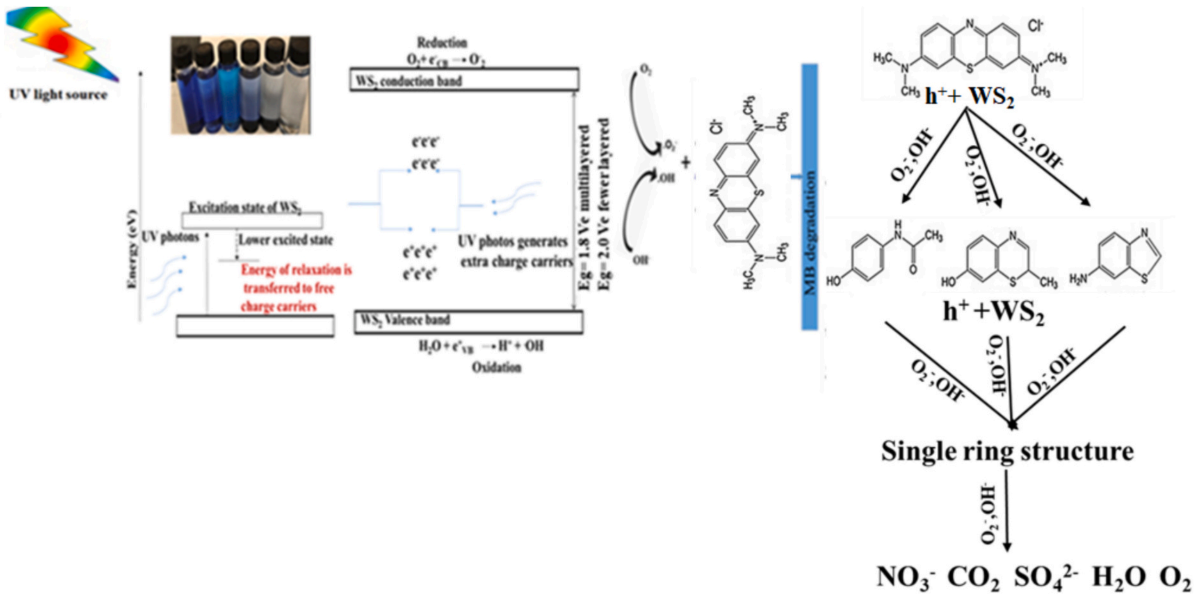

Fig. 10. Photocatalytic degradation mechanism of MB under UV-light irradiation using G-WS_2 and B-WS_2 as a photocatalyst.

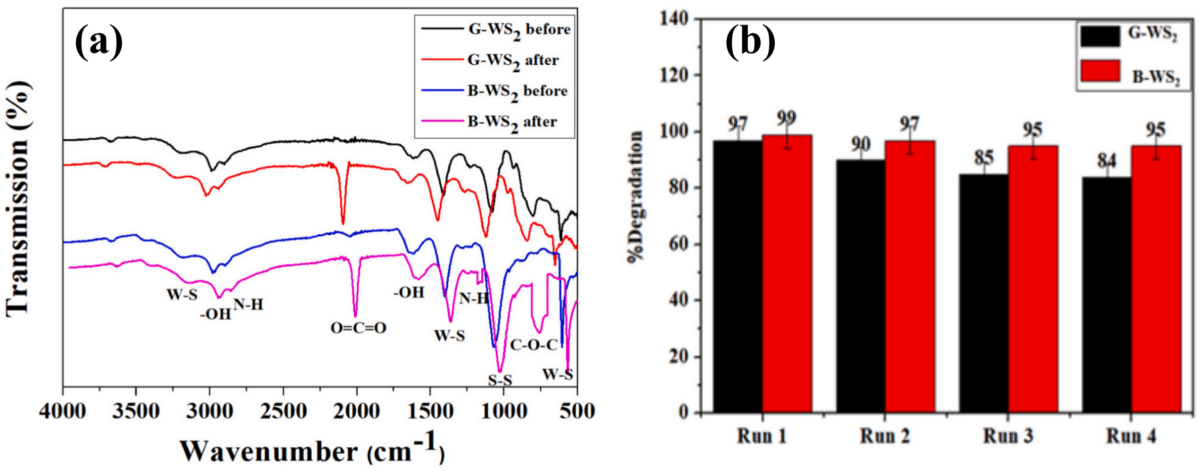

Fig. 11. (a) FTIR of the photocatalyst before and after (b) Reusability of the spent G-WS_2 and B-WS_2 for MB degradation. (Concentration 200 mg/L, catalyst mass 40 mg, volume 40 mL, time 60 min).

CRediT authorship contribution statement

Lizzie Mampane: Writing – review & editing, Writing – original draft, Visualization, Validation, Methodology, Investigation, Formal analysis, Conceptualization. **Bulelwa Ntsendwana:** Writing – review & editing, Writing – original draft, Methodology, Investigation, Conceptualization. **William Moloto:** Methodology, Investigation. **Sivuyisiwe Mapukata:** Methodology, Formal analysis. **Themba Ntuli:** Methodology, Investigation. **Nosipho Moloto:** Writing – review & editing, Supervision, Methodology, Investigation, Formal analysis, Conceptualization. **Lucky Sikhwivhilu:** Writing – review & editing, Project administration, Methodology, Investigation, Funding acquisition, Formal analysis, Conceptualization.

Funding

his research was funded by the Department of Science, Technology and Innovation (DSTI)/Mintek Nanotechnology Innovation Centre, ADE 42505 and the University of Witwatersrand, South Africa.

Declaration of competing interest

The authors declare that they have no known competing financial interests or personal relationships that could have appeared to influence the work reported in this paper.

Data availability

Data will be made available on request.

References

[1] L.C. Giudice, et al., Climate change, women's health, and the role of obstetricians and gynecologists in leadership, Int. J. Gynecol. Obstet. 155 (3) (2021) 345–356, https://doi.org/10.1002/ijgo.13958.

[2] E.K. Nti, et al., Water pollution control and revitalization using advanced technologies: uncovering artificial intelligence options towards environmental health protection, sustainability and water security, Heliyon 9 (7) (2023), https://doi.org/10.1016/j.heliyon.2023.e18170.

[3] L. Taneja, S. Raghav, C. Kochar, P.K. Yadav, S. Swarupa Tripathy, Effective remediation of fluoride from drinking water using cerium-silver oxide composite incorporated with reduced graphene oxide, J. Water Process. Eng. 44 (July) (2021), https://doi.org/10.1016/j.jwpe.2021.102369.

[4] J. Fito, et al., Adsorption of methylene blue from textile industrial wastewater using activated carbon developed from Rumex abyssinicus plant, Sci. Rep. 13 (1) (2023) 1–17, https://doi.org/10.1038/s41598-023-32341-w.

[5] M.A. Hassaan, M.A. El-Nemr, M.R. Elkatory, S. Ragab, V.C. Niculescu, A. El Nemr, Principles of photocatalysts and their different applications: A review 381, Springer International Publishing, 2023, https://doi.org/10.1007/s41061-023-00444-7, 6.

[6] J.B. Batchamen Mougnol, F. Waanders, S.K.O. Ntwampe, E. Fosso-Kankeu, A.R. Al Alili, Synthesis of eco-friendly ZnO-based heterophotocatalysts with enhanced properties under visible light in the degradation of organic pollutants, Environ. Syst. Res. 11 (1) (2022), https://doi.org/10.1186/s40068-022-00271-7.

[7] M. Naushad, R. Saravanan, K. Raju, Nanomaterials for Sustainable Energy and Environmental Remediation, Nanomaterials Sustain. Energy Env. Remediation (2020) 1–371, https://doi.org/10.1016/B978-0-12-819355-6.01001-3.

[8] F. Ai, X. Yin, R. Hu, H. Ma, W. Liu, Research into the super-absorbent polymers on agricultural water, Agric. Water Manag. 245 (June 2020) (2021) 1–7, https://doi.org/10.1016/j.agwat.2020.106513.

[9] G.S. Shanker, A. Biswas, S. Ogale, 2D materials and their heterostructures for photocatalytic water splitting and conversion of CO2 to value chemicals and fuels, IOP Publishing Ltd. (Apr. 01, 2021), https://doi.org/10.1088/2515-7655/abdcab.

[10] P. Kumbhakar, et al., Prospective applications of two-dimensional materials beyond laboratory frontiers: a review, iScience 26 (5) (2023) 1–24, https://doi.org/10.1016/j.isci.2023.106671.

[11] F.M. Pinto, et al., Recent Advances in Layered MX2-Based Materials (M = Mo, W and X = S, Se, Te) for Emerging Optoelectronic and Photo(electro)catalytic Applications, Multidisciplinary Digital Publishing Institute (MDPI), Jun. 01, 2024, https://doi.org/10.3390/catal14060388.

[12] A. Yousef, Z. Thiehmed, R. Abdul Shakoor, T. Altahtamouni, Recent Progress in WS2-based nanomaterials employed for photocatalytic water treatment, Catalysts 12 (10) (2022) 1–42, https://doi.org/10.3390/catal12101138.

[13] A. Yousef, Z. Thiehmed, R. Abdul Shakoor, T. Altahtamouni, Recent progress in WS2-based nanomaterials employed for photocatalytic water treatment, MDPI (Oct. 01, 2022), https://doi.org/10.3390/catal12101138.

[14] T. Bavani, M. Preeyanghaa, B. Neppolian, J. Madhavan, D. Balaji, ChemPhotoChem Supporting Information A Hybrid S-Scheme WS 2 /BiOI Heterojunction Photocatalyst for Wastewater Treatment, 2025.

[15] T. Fatima, S. Husain, J. Narang, M. Khanuja, N.P. Shetti, K.R. Reddy, Novel tungsten disulfide (WS2) nanosheets for photocatalytic degradation and electrochemical detection of pharmaceutical pollutants, J. Water Process Eng. 47 (Jun. 2022), https://doi.org/10.1016/j.jwpe.2022.102717.

[16] X. Xie, et al., A WS2/sepiolite composite with highly dispersed WS2 nanosheets for photocatalytic wastewater treatment, Appl. Clay Sci. 228 (Oct. 2022), https://doi.org/10.1016/j.clay.2022.106576.

[17] Z.X. Wei, W.Q. Huang, L. Xu, W. Hu, P. Peng, G.F. Huang, Dual functions of 2D WS2 and MoS2-WS2 monolayers coupled with a Ag3PO4 photocatalyst, Semicond. Sci. Technol. 31 (9) (Aug. 2016), https://doi.org/10.1088/0268-1242/31/9/095013.

[18] A.G. Alhamzani, et al., Fabrication of layered In2S3/WS2 heterostructure for enhanced and efficient photocatalytic CO2 reduction and various paraben degradation in water, Chemosphere 322 (May 2023), https://doi.org/10.1016/j.chemosphere.2023.138235.

[19] V. Shinde, P. Tanwade, T. Katayama, A. Furube, B. Sathe, P. Koinkar, Ternary composite WS2/GO/au synthesized from laser ablation and hydrothermal method for photo- and electro-chemical degradation of methylene blue dye, Surfaces Interfaces 46 (Mar. 2024), https://doi.org/10.1016/j.surfin.2024.104067.

[20] Y. Dai, et al., Liquid exfoliation and electrochemical properties of WS 2 Nanosheets, J. Nanosci. Nanotechnol. 18 (5) (Nov. 2017) 3165–3170, https://doi.org/10.1166/jnn.2018.14689.

[21] T.A.J. Loh, D.H.C. Chua, A.T.S. Wee, One-step synthesis of few-layer WS2 by pulsed laser deposition, Sci. Rep. 5 (Dec. 2015), https://doi.org/10.1038/srep18116.

[22] J.R. Brent, N. Savjani, P. O'Brien, Synthetic approaches to two-dimensional transition metal dichalcogenide nanosheets, Elsevier Ltd (Aug. 01, 2017), https://doi.org/10.1016/j.pmatsci.2017.06.002.

[23] P. Stehlík, Conventional Versus Specific Types of Heat Exchangers in the Case of Polluted Flue Gas as the Process Fluid - a Review, Elsevier Ltd., 2011, https://doi.org/10.1016/j.applthermaleng.2010.06.013.

[24] P. Koinkar, et al., Effect of nanosecond and femtosecond pulse laser on the formation of WS2 nanostructures and field emission characteristics, in: Modern Physics Letters B, World Scientific Publishing Co. Pte Ltdin, May 2019, https://doi.org/10.1142/S0217984919400141.

[25] K. Wu, P. Koinkar, A. Furube, Preparation of WS2–TiO2–au using hydrothermal synthesis for photocatalysis under visible light, Int. J. Mod. Phys. B 35 (14n16) (Jun. 2021) 2140046, https://doi.org/10.1142/S0217979221400464.

[26] P. Koinkar, et al., Effect of nanosecond and femtosecond pulse laser on the formation of WS2 nanostructures and field emission characteristics, Mod. Phys. Lett. B 33 (14n15) (Apr. 2019) 1940014, https://doi.org/10.1142/S0217984919400141.

[27] S. Ott, M. Lakmann, C. Backes, Impact of pretreatment of the bulk starting material on the efficiency of liquid phase exfoliation of WS2, Nanomaterials 11 (5) (May 2021), https://doi.org/10.3390/nano11051072.

[28] G. Yang, C. Zhu, D. Du, J. Zhu, Y. Lin, Graphene-like two-dimensional layered nanomaterials: applications in biosensors and nanomedicine, Nanoscale 7 (34) (Sep. 2015) 14217–14231, https://doi.org/10.1039/c5nr03398e.

[29] S. Ratha, C.S. Rout, Supercapacitor electrodes based on layered tungsten disulfide-reduced graphene oxide hybrids synthesized by a facile hydrothermal method, ACS Appl. Mater. Interfaces 5 (21) (Nov. 2013) 11427–11433, https://doi.org/10.1021/am403663f.

[30] X.H. Zhang, H. Tan, Z. Fan, M.Z. Ge, X. Ye, M.Q. Xue, Synthesis and electrochemical performance of ultrathin ws 2 nanosheets, 2017.

[31] X. Zhang, et al., Synthesis of ultrathin WS2 Nanosheets and their Tribological properties as lubricant additives, Nanoscale Res. Lett. 11 (1) (2016), https://doi.org/10.1186/s11671-016-1659-3.

[32] Y. Sun, et al., Atomically thick bismuth selenide freestanding single layers achieving enhanced thermoelectric energy harvesting, J. Am. Chem. Soc. 134 (50) (2012) 20294–20297, https://doi.org/10.1021/ja3102049.

[33] L. Haghighi, N. Haghnazari, C. Karami, Tungsten disulfide quantum dots (WS2 QDs) as a fluorescence probe for detection of dopamine (DA), J. Mater. Sci. Mater. Electron. 32 (24) (2021) 28042–28050, https://doi.org/10.1007/s10854-021-07098-5.

[34] B. Smith, Infrared spectral interpretation: a systematic approach, Infrared Spectral Interpretation: Syst. Approach (2018) 1–304, https://doi.org/10.1201/9780203750841.

[35] P. Pal, in: P. Pal (Ed.), Chapter 6—Industry-Specific Water Treatment: Case Studies, Butterworth-Heinemann: Oxford, UK, 2017.

[36] I.H. Kwak, I.S. Kwon, J.H. Lee, Y.R. Lim, J. Park, Chalcogen-vacancy group VI transition metal dichalcogenide nanosheets for electrochemical and photoelectrochemical hydrogen evolution, J. Mater Chem. C Mater 9 (1) (2021) 101–109.

[37] R. Sharma, N. Chadha, P. Saini, Determination of defect density, crystallite size and number of graphene layers in graphene analogues using X-ray diffraction and Raman spectroscopy, Indian J. Pure Appl. Phys. 55 (9) (2017) 625–629.

[38] Asiva Noor Rachmayani, "No 主観的健康感を中心とした在宅高齢者における 健康関連指標に関する共分散構造分析Title," p. 6, 2015, doi: https://doi.org/10.1002/adsu.202000068.This.

[39] R. Swaminathan, P. Pazhamalai, V. Mohan, K. Krishnamoorthy, S.J. Kim, Topochemically prepared tungsten disulfide nanostructures as a novel pseudocapacitive electrode for high performance supercapacitor, J. Colloid Interface Sci. 652 (PA) (2023) 845–855, https://doi.org/10.1016/j.jcis.2023.07.143.

[40] F. Huang, J.K. Jian, R. Wu, Few-layer thick WS2 nanosheets produced by intercalation/exfoliation route, J. Mater. Sci. 51 (22) (2016) 10160–10165, https://doi.org/10.1007/s10853-016-0243-7.

[41] Y.Q. Qin, Y.Q. Peng, W.F. Yang, Y. Wang, J.W. Cui, Y. Zhang, Ultrathin exfoliated WS2 nanosheets in low-boiling-point solvents for high-efficiency hydrogen evolution reaction, in: IOP Conference Series: Materials Science and Engineering, Institute of Physics Publishing, Mar. 2020, https://doi.org/10.1088/1757-899X/770/1/012079.

[42] M. Piao, et al., Hydrothermal synthesis of stable metallic 1T phase WS2 nanosheets for thermoelectric application, Nanotechnology 29 (2) (Jan. 2018), https://doi.org/10.1088/1361-6528/aa9bfe.

[43] E. Del Corro, et al., Atypical exciton-phonon interactions in WS2 and WSe2 monolayers revealed by resonance Raman spectroscopy, Nano Lett. 16 (4) (Apr. 2016) 2363–2368, https://doi.org/10.1021/acs.nanolett.5b05096.

[44] S. Najmaei, Z. Liu, P.M. Ajayan, J. Lou, Thermal effects on the characteristic Raman spectrum of molybdenum disulfide (MoS 2) of varying thicknesses, Appl. Phys. Lett. 100 (1) (Jan. 2012), https://doi.org/10.1063/1.3673907.

[45] R.K. Jha, P.K. Guha, Liquid exfoliated pristine WS2 nanosheets for ultrasensitive and highly stable chemiresistive humidity sensors, Nanotechnology 27 (47) (2016) 475503.

[46] J.A. Desai, N. Adhikari, A.B. Kaul, Chemical exfoliation efficacy of semiconducting WS2 and its use in an additively manufactured heterostructure graphene-WS2-graphene photodiode, RSC Adv. 9 (44) (2019) 25805–25816, https://doi.org/10.1039/c9ra03644j.

[47] A. Berkdemir, et al., Identification of individual and few layers of WS2 using Raman spectroscopy, Sci. Rep. 3 (2013) 1–8, https://doi.org/10.1038/srep01755.

[48] P. Sehrawat Abid, S.S. Islam, Broadband photodetection in wide temperature range: layer-by-layer exfoliation monitoring of WS2 bulk using microscopy and spectroscopy, J. Appl. Phys. 125 (15) (2019), https://doi.org/10.1063/1.5080922.

[49] Z.A. Alothman, A review: fundamental aspects of silicate mesoporous materials, Materials 5 (12) (2012) 2874–2902, https://doi.org/10.3390/ma5122874.

[50] F.H. Margha, E.K. Radwan, M.I. Badawy, T.A. Gad-Allah, Bi2O3-BiFeO3Glass-ceramic: controllable β−/γ-Bi2O3Transformation and application as magnetic solar-driven Photocatalyst for water decontamination, ACS Omega 5 (24) (Jun. 2020) 14625–14634, https://doi.org/10.1021/acsomega.0c01307.

[51] H. Song, et al., Modification of WS 2 nanosheets with controllable layers via oxygen ion irradiation, Appl. Surf. Sci. 439 (May 2018) 240–245, https://doi.org/10.1016/j.apsusc.2018.01.019.

[52] E. Moradpur-Tari, R. Sarraf-Mamoory, A. Yourdkhani, Structural, electronic, and electrochemical studies of WS2 phases using density functional theory and machine learning, Phys. B Condens. Matter 650 (Feb. 2023), https://doi.org/10.1016/j.physb.2022.414568.

[53] A. Roy, P. Kalita, B. Mondal, Structural, spectroscopic and electrical properties of liquid phase exfoliated few layered two-dimensional tungsten disulfide (WS2) using anionic surfactant, J. Mater. Sci. Mater. Electron. 34 (3) (Jan. 2023), https://doi.org/10.1007/s10854-022-09687-4.

[54] S. Ghosh, et al., Cathodoluminescence in single and multiwall WS2nanotubes: Evidence for quantum confinement and strain effect, Appl. Phys. Rev. 7 (4) (Dec. 2020), https://doi.org/10.1063/5.0019913.

[55] J.A. Desai, N. Adhikari, A.B. Kaul, Chemical exfoliation efficacy of semiconducting WS2 and its use in an additively manufactured heterostructure graphene-WS2-

graphene photodiode, RSC Adv. 9 (44) (2019) 25805–25816, https://doi.org/10.1039/c9ra03644j.

[56] J. Liang, et al., Reversible electron doping in monolayer WS2 via a chemical strategy, 2d Mater 6 (2) (Jan. 2019), https://doi.org/10.1088/2053-1583/aafa48.

[57] D.R. Hang, et al., Facile bottom-up preparation of WS2-based water-soluble quantum dots as luminescent probes for hydrogen peroxide and glucose, Nanoscale Res. Lett. 14 (1) (Dec. 2019), https://doi.org/10.1186/s11671-019-3109-5.

[58] S. Sharma, S. Bhagat, J. Singh, R.C. Singh, S. Sharma, Excitation-dependent photoluminescence from WS2 nanostructures synthesized via top-down approach, J. Mater. Sci. 52 (19) (Oct. 2017) 11326–11336, https://doi.org/10.1007/s10853-017-1303-3.

[59] S. Khan, T. Noor, N. Iqbal, L. Yaqoob, Photocatalytic Dye Degradation from Textile Wastewater: A Review, Am. Chem. Soc. (May 21, 2024), https://doi.org/10.1021/acsomega.4c00887.

[60] S.G. Shelar, V.K. Mahajan, S.P. Patil, G.H. Sonawane, Effect of doping parameters on photocatalytic degradation of methylene blue using Ag doped ZnO nanocatalyst, SN Appl. Sci. 2 (5) (2020), https://doi.org/10.1007/s42452-020-2634-2.

[61] L. Karger, et al., The role of additives in suppressing the degradation of liquid-exfoliated WS2 monolayers, Adv. Mater. 33 (42) (Oct. 2021), https://doi.org/10.1002/adma.202102883.

[62] B. Wang, S. Shen, S.S. Mao, Black TiO2 for solar hydrogen conversion, J. Mater. 3 (2) (2017) 96–111, https://doi.org/10.1016/j.jmat.2017.02.001.

[63] P.O. Oladoye, T.O. Ajiboye, E.O. Omotola, O.J. Oyewola, Methylene blue dye: Toxicity and potential elimination technology from wastewater, Elsevier B.V, Dec. 01, 2022, https://doi.org/10.1016/j.rineng.2022.100678.

[64] D.O. Ozcan, M.C. Hendekci̇, B. Ovez, Enhancing the adsorption capacity of organic and inorganic pollutants onto impregnated olive stone derived activated carbon, Heliyon 10 (12) (Jun. 2024), https://doi.org/10.1016/j.heliyon.2024.e32792.

[65] N.F. Jaafar, A.A. Jalil, S. Triwahyono, A. Ripin, M.W. Ali, Significant effect of ph on photocatalytic degradation of organic pollutants using semiconductor catalysts, J. Teknol. 78 (8–3) (2016) 7–12, https://doi.org/10.11113/jt.v78.9559.

[66] M. Kosmulski, pH-dependent surface charging and points of zero charge II. Update, J. Colloid Interface Sci. 275 (1) (Jul. 2004) 214–224, https://doi.org/10.1016/j.jcis.2004.02.029.

[67] M. Kosmulski, The pH dependent surface charging and points of zero charge. X. Update, Elsevier B.V., Sep. 01, 2023, https://doi.org/10.1016/j.cis.2023.102973.

[68] F. Chen, T. Ma, T. Zhang, Y. Zhang, H. Huang, Atomic-Level Charge Separation Strategies in Semiconductor-Based Photocatalysts, John Wiley and Sons Inc, Mar. 01, 2021, https://doi.org/10.1002/adma.202005256.

[69] Y. Han, L.H. Spangler, Use of isosbestic points for determination of quantum efficiency in transient absorption spectroscopy, J. Phys. Chem. A 106 (9) (Mar. 2002) 1701–1707, https://doi.org/10.1021/jp013717x.

[70] S. Sehar, et al., Shape-controlled synthesis of cerium oxide nanoparticles for efficient dye photodegradation and antibacterial activities, Appl. Organomet. Chem. 35 (1) (Jan. 2021), https://doi.org/10.1002/aoc.6069.

[71] S. Shahabuddin, S. Mehmood, I. Ahmad, N. Sridewi, Synthesis and characterization of 2D-WS2 incorporated polyaniline nanocomposites as photo catalyst for methylene blue degradation, Nanomaterials 12 (12) (Jun. 2022), https://doi.org/10.3390/nano12122090.

[72] W. Ashraf, T. Fatima, K. Srivastava, M. Khanuja, Superior photocatalytic activity of tungsten disulfide nanostructures: role of morphology and defects, Appl. Nanosci. (Switzerland) 9 (7) (Oct. 2019) 1515–1529, https://doi.org/10.1007/s13204-019-00951-4.

[73] W. Ashraf, A. Khan, S. Bansal, M. Khanuja, Mechanical ball milling: a sustainable route to induce structural transformations in tungsten disulfide for its photocatalytic applications, Physica. E Low Dimens. Syst. Nanostruct. 140 (Jun. 2022), https://doi.org/10.1016/j.physe.2022.115152.

[74] R. Sharma, S. Uma, A. Verma Singh, M. Khanuja, Visible light induced bactericidal and photocatalytic activity of hydrothermally synthesized BiVO4 nano-octahedrals, J. Photochem. Photobiol. B 162 (Sep. 2016) 266–272, https://doi.org/10.1016/j.jphotobiol.2016.06.035.

[75] H.Y. Ma, L. Zhao, L.H. Guo, H. Zhang, F.J. Chen, W.C. Yu, Roles of reactive oxygen species (ROS) in the photocatalytic degradation of pentachlorophenol and its main toxic intermediates by TiO2/UV, J. Hazard. Mater. 369 (May 2019) 719–726, https://doi.org/10.1016/j.jhazmat.2019.02.080.

[76] Y. Cao, Q. Li, W. Wang, Construction of a crossed-layer-structure MoS2/g-C3N4 heterojunction with enhanced photocatalytic performance, RSC Adv. 7 (10) (2017) 6131–6139, https://doi.org/10.1039/c6ra26925g.